Measurement of the velocity field in parametrically excited solitary waves

Leonardo Gordillo[1,2,†] and Nicolás Mujica[1]

[1]Departamento de Física, Facultad de Ciencias Físicas y Matemáticas, Universidad de Chile,
Casilla 487-3, Santiago, Chile

[2]Laboratoire 'Matière et Systèmes Complexes' (MSC), UMR 7057 CNRS, Université Paris 7 Diderot,
75205 Paris CEDEX 13, France

Parametrically excited solitary waves emerge as localized structures in high-aspect-ratio free surfaces subject to vertical vibrations. Herein, we provide the first experimental characterization of the hydrodynamics of these waves using particle image velocimetry. We show that the underlying velocity field of parametrically excited solitary waves is primarily composed of a subharmonic oscillatory component. Our results confirm the accuracy of Hamiltonian models with added dissipation in describing this field. Remarkably, our measurements also uncover the onset of a streaming velocity field which we show to be as important as other crucial nonlinear terms in the current theory. Using vorticity equations, we show that the streaming pattern arises from the coupling of the potential bulk flow with the oscillating boundary layers on the vertical walls. Numerical simulations provide good agreement between this model and experiments.

Key words: parametric instability, solitary waves, waves/free-surface flows

1. Introduction

Parametric instabilities in spatially extended systems can generate waves by their resonance with an external driving force, providing a universal mechanism to generate structures in dissipative systems. In hydrodynamics, these structures satisfy a simple rule: energy losses due to viscous effects are compensated by external energy injection, e.g. by means of vertical vibrations. This balance can create extended or solitary structures that remain stable as long as the system is driven by the external force. In particular, solitary waves emerge in high-aspect-ratio free surfaces subject to vertical vibrations as a result of exciting the system at twice the frequency of the first transverse mode. They become stable only after perturbing the free surface. These waves keep the sloshing motion features of the first transverse mode, but rather than involving the whole surface, their motion is highly localized in the longitudinal direction (Wu, Keolian & Rudnick 1984). This solitary wave is usually referred as a non-propagating hydrodynamic soliton or a parametrically excited solitary wave. In contrast to classical hydrodynamic solitons, the spatial envelopes of these

structures are stable and do not propagate. Remarkably, this behaviour can be found in several hydrodynamic systems: oscillons in the Faraday configuration (Arbell & Fineberg 2000) or solitary waves in vibrated Hele-Shaw cells (Rajchenbach, Leroux & Clamond 2011) display spatial envelopes with similar spatiotemporal features.

Parametrically excited solitary waves are modelled in terms of the parametric dissipative nonlinear Schrödinger equation (pdNLSe), derived by Miles (1984*b*). This equation captures the minimum requirements for parametrically sustained one-dimensional solitary structures. Hence, its scope goes far beyond hydrodynamics (see e.g. Barashenkov, Bogdan & Korobov 1991; Denardo *et al.* 1992). Recent studies have been focused on providing an exhaustive analysis of the pdNLSe using mathematical and numerical techniques. Experiments have also been used for this purpose (see Zhang, Wang & Tao 2007; Clerc *et al.* 2011; Gordillo *et al.* 2011). Despite all of this focus, fundamental issues such as the validity of the approximations that yield the pdNLSe have remained unaddressed. Systematic comparisons between predictions and measurements are rare (Chen, Tu & Wei 1999). Furthermore, all of the experimental characterizations that can be found in the literature have been achieved using a single technique, i.e. by tracking the free surface, a measurement useful for outlining solitary-wave stability and interaction laws but blind to potential subsurface phenomena. This is a critical issue, since most steps involved in the pdNLSe derivation rely strongly on hypotheses from fluid dynamics. It is thus fundamental to uncover the velocity field beneath the surface for a comprehensive experimental analysis of parametrically excited solitary waves.

In this article, we present experimental results concerning parametrically excited solitary waves with a focus on the hydrodynamics. We have measured the velocity fields that support the localized cross-waves using particle image velocimetry (PIV). The article is organized as follows. In §2, we outline the pdNLSe theoretical model. In §3, we briefly describe the experimental set-up. A summary of our most significant experimental results can be found in §4. Finally, discussion and conclusions, including comparisons with pdNLSe theoretical predictions, are given in §5.

2. Theory

Consider a fluid layer of depth d in an infinite channel of breadth b. The channel is oriented along the x axis (walls at $y = \pm b/2$ and $z = -d$) and is forced to oscillate vertically at frequency 2ω and acceleration amplitude Γ_0. The vertical acceleration of the channel is accordingly $\Gamma(t) = -\Gamma_0 \cos 2\omega t$. Let us assume that ω approaches ω_{01}, the first-transverse-mode frequency, so the $(0, 1)$ mode is parametrically excited. The linear theory of gravity waves for inviscid flows provides a good estimation for the $(0, 1)$-mode frequency, $\omega_{01} = \sqrt{gk\tau}$, where g is the acceleration of gravity, $k = \pi/b$ is the wavenumber and $\tau \equiv \tanh kd$. The parametric forcing can thus be characterized in terms of two dimensionless parameters: the detuning $\nu = (\omega^2/\omega_{01}^2 - 1)/2$ and the normalized acceleration amplitude $\gamma = \Gamma_0/(4g)$.

Free-surface waves in constant-depth inviscid flows are known to be Hamiltonian (cf. Miles 1977). This can be used as a point of departure for deriving amplitude equations in such systems. However, realistic set-ups are not conservative, and external forcing is required to create such structures. In any case, although viscous effects are neglected *a priori* in Hamiltonian formulations, the addition of linear dissipation in amplitude equations seems to be sufficient for modelling slightly viscous flows (Miles 1976). The reason is simple: in this kind of flow, the motion is close to inviscid everywhere except in the boundary layers. Energy is thus dissipated without affecting

the general features of the waves (cf. Miles 1967). For instance, the decay rate for the $(0, 1)$ mode, α_{01}, can be estimated from boundary layer analysis (Miles 1984*b*). In our problem, this provides an extra dimensionless parameter, the damping rate $\mu = \alpha_{01}/\omega_{01}$.

Using the stated hypotheses, it can be shown rigorously that the first transverse mode in an infinite channel can be modelled with (Miles 1984*b*)

$$\mathrm{i}\,(\partial_T \psi + \mu \psi) = \nu \psi + 2\,|\psi|^2\,\psi + \partial_{XX}\psi + \gamma \overline{\psi}, \qquad (2.1)$$

which is the pdNLSe. It should be noticed that this equation is written in terms of the dimensionless variables $T = \omega_{01}t$ and $X = b_s^{-1/2}kx$, where t stands for time, x for the longitudinal spatial coordinate and $b_s = [1 + kd(1 - \tau^2)/\tau]/4$. The complex field $\psi(X, T)$ contains the slow spatiotemporal modulation of the first transverse mode. In general, the deformation at the free surface, $\eta(x, y, t)$, and the velocity potential inside the fluid, $\Phi(x, y, z, T)$, are related to $\psi(X, T)$ by

$$\eta\,(x, y, t) \;=\; \mathrm{Re}\{a_s \psi\,(X, T)\exp \mathrm{i}\omega t\}\sin ky, \qquad (2.2)$$

$$\Phi\,(x, y, z, t) \;=\; \mathrm{Im}\{a_s \psi\,(X, T)\exp \mathrm{i}\omega t\}\,\frac{g \sin ky \cosh k\,(z + d)}{\omega_{01}\cosh kd}, \qquad (2.3)$$

where $a_s^2 = 128k^{-2}/(6\tau^2 - 5 + 16\tau^{-2} - 9\tau^{-4})$.

Just like their propagating counterparts, non-propagating hydrodynamic solitons arise from a subtle balance between linearities, nonlinearities and dispersion. Parametrically excited solitary waves can be found by assuming solutions of the form $\psi(X, T) = \rho(X)\mathrm{e}^{-\mathrm{i}\theta}$. Straightforward calculations show the onset of a subcritical instability for $\gamma > \mu$ and $\nu < 0$ with two families of solutions. One family of solutions is always unstable, whereas the other one, given by

$$\psi\,(X, T) = \pm \mathrm{i}\delta\,\mathrm{sech}\,[\delta\,(X - X_0)]\,\mathrm{e}^{\mathrm{i}/2\sin^{-1}\,(\mu/\gamma)}, \qquad (2.4)$$

is stable whenever $\gamma^2 < \nu^2 + \mu^2$, and provided that $\delta^2 = -\nu + (\gamma^2 - \mu^2)^{1/2}$ (see Laedke & Spatschek 1991). The free parameter x_0 comes out from a constant of integration and represents the position of the centre of mass of the envelope. Additionally, (2.4) consists of two solutions with opposite sign. This is consistent with experimental observations of a sort of soliton polarity, a crucial feature for pair interactions (Wang & Wei 1994; Wang *et al.* 1996; Clerc *et al.* 2009). Equation (2.1) also supports cnoidal and dnoidal families of solutions (cf. Miles 1984*b*; Umeki 1991). Furthermore, a change of sign in its nonlinear cubic term gives rise to the kink-type solutions observed by Denardo *et al.* (1990). This is achieved, for instance, by decreasing the depth of the fluid layer (see also Miles 1984*b*, pp. 455–456).

3. Experimental set-up

We ran our experiments in an acrylic basin attached to an electromagnetic shaker (see figure 1). The trough of length $l = 19.05$ cm and breadth $b = 2.54$ cm was filled with an aqueous solution to a depth $d = 2.00$ cm. The aqueous solution contained 2 ml of Photoflo to improve wall wetting (Wu *et al.* 1984), as well as a small amount of KBr (13 % in mass concentration) to increase the fluid density. The solution density matched that of the PIV particles, 1.1 g cm^{-3}, so that particle settling became noticeable only after several hours (kinematic viscosity was also reduced by approximately 15 %, cf. Lide, 2004). The acceleration of the basin was registered using a piezoelectric accelerometer and a lock-in amplifier referenced externally to
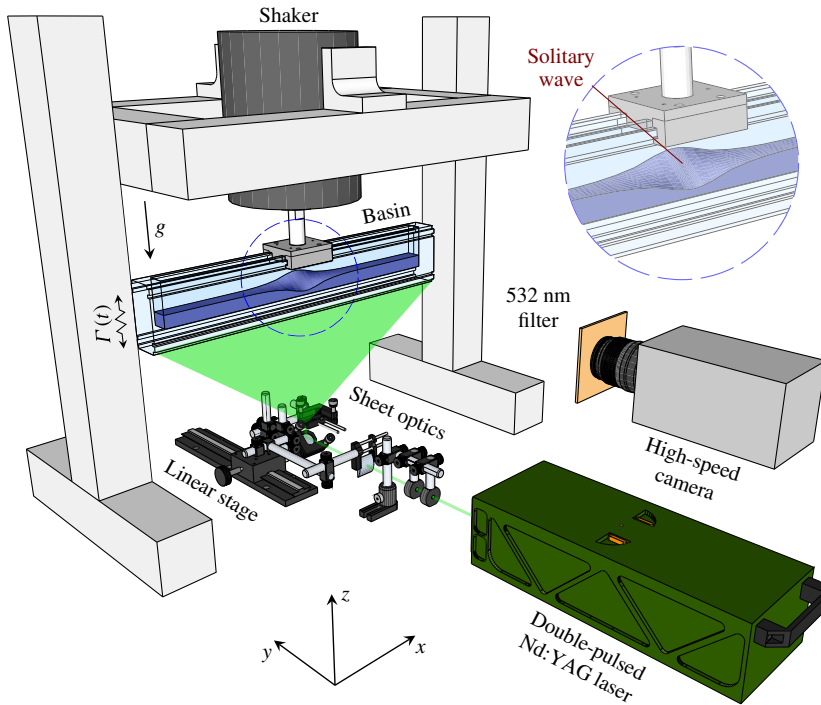
FIGURE 1. (Colour online) General scheme of the set-up. Solitary waves can be created in the basin fluid after injecting energy through vertical vibrations. The fluid is seeded with fluorescent particles and illuminated by a vertical laser sheet moveable in the y direction. PIV digital processing allows us to measure the velocity field in the x–z plane at fixed y_s.

the input shaker signal. Parametrically excited solitary waves were observed when the system was accelerated vertically as $\Gamma(t) = -\Gamma_0 \cos(2\pi ft)$, at frequencies f slightly below 11 Hz and acceleration amplitudes Γ_0 of approximately $0.1g$. The frequency threshold was very close to double the experimental first transverse-mode frequency, $f_{0,1} = 5.49$ Hz, which was obtained by measuring the linear surface response using a capacitive sensor and a spectrum analyser in frequency-sweep mode (for more details, cf. Gordillo 2012).

The PIV particles inside the fluid (carboxy-modified acrylate resin, $\varnothing = 15$ µm) were illuminated using a double-pulsed Nd:YAG laser (70 mJ per pulse) and a laser sheet generator. We placed the latter on a linear translational stage so that the sheet position along the fluid layer y could be easily adjusted. The laser sheet thickness inside the fluid was 2 mm. We remark that illumination from the bottom is the only type compatible with PIV and measurement requirements. Unfortunately, due to the back and forth sloshing of the solitary waves (see the zoomed window in figure 1), the free surface reflected a huge amount of light in the y direction. To avoid this, we used fluorescent PIV particles (absorption and emission peaks at 550 and 580 nm respectively) and blocked reflections with a longpass optical filter whose cutoff matched the light-source wavelength (532 nm).

Images were acquired using a high-speed camera providing an imaging region of 2560 pixels × 512 pixels (20.0 cm × 4.0 cm). We synchronized the laser double pulses ($\Delta t = 10$ ms) with the motion of the solitary wave at a fixed phase θ_s.

Since the solitary wave sloshed at $f/2$ and at a fixed phase with respect to the shaker input signal, the latter signal was used as the reference. The frames were acquired synchronously with the laser pulses. Each run consisted of 200 image pairs for fixed sheet position y_s and solitary-wave phase θ_s. A set of 36 different θ_s values were analysed throughout the full solitary-wave cycle. Furthermore, 10 laser sheet positions y_s across the fluid layer were analysed for a fixed phase, $\theta_s = \pi$, at which the free-surface deformation was zero and the velocity was maximal on the front wall.

Image processing was performed using our own Matlab code with classical PIV digital techniques. As the image sequences included a moving boundary, we required an automatic algorithm for boundary detection. We achieved this by using a Radon-transform-based method from Sanchis & Jensen (2011) on averaged same-phase samples. Similarly, background and illumination issues were corrected using statistics-based images. The calculated boundaries were then used for creating binary masks, which in turn were used in a multi-pass interrogation PIV scheme. The minimum interrogation-window size was 16 pixels × 16 pixels (1.25 mm × 1.25 mm). The results presented here were averaged over the 200 samples in the correlation-function space to improve the signal-to-noise ratio.

4. Results

As a consequence of the pulsed-laser synchronization, the image sequences are composed of a series of double fast snapshots ($\Delta t = 10$ ms) captured every soliton period ($\Delta t' = 2/f$). This temporal scheme provides sets of time-resolved velocity fields for a fixed phase between the external forcing and the soliton oscillation. By tuning this phase, the velocity field during the whole cycle can be found. The resulting velocity field $\boldsymbol{u} = (u, v, w)$ is mainly oscillatory in time, similar to those of stationary waves. However, the temporal scheme provides more information. A simple inspection of sequences shows that after one cycle, seeding particles do not return to their position from the preceding cycle. If one frame is skipped such that the temporal scheme is stroboscopic, it is easy to notice that particles are constantly streamed. The effect of this streaming velocity field $\overline{\boldsymbol{u}} = (\overline{u}, \overline{v}, \overline{w})$ becomes perceptible in particle trajectories only after one or several cycles. In this sense, the instantaneous velocity field $\boldsymbol{u}$ can be considered as the sum of two components: the oscillatory part, $\widetilde{\boldsymbol{u}} = (\widetilde{u}, \widetilde{v}, \widetilde{w})$, and the streaming one, $\overline{\boldsymbol{u}}$.

In figure 2, we depict the velocity field inside the bulk of a parametrically excited solitary wave at the phase $\theta_s = \pi$. Figures 2(*a*) and (2*b*) display respectively the instantaneous and streaming velocity fields in the *x*–*z* plane for a fixed $y_s = -1.07$ cm. The driving frequency and amplitude for these waves were $f = 10.9$ Hz and $\Gamma_0 = 0.096g$. The solitary-wave envelope is in the centre of the basin ($x_0 = 0$ in (2.4)). Corresponding movies can be viewed in the supplementary material available online at http://dx.doi.org/10.1017/jfm.2014.416.

In figure 3, we include side views (*y*–*z* plane) of the velocity field captured at the same phase $\theta_s = \pi$. For this sequence, the basin was rotated by 90° in the *x*–*y* plane (the axes remained fixed to the basin). To obtain a full view of the velocity field, we used a half solitary wave pinned at $x_0 = l/2$ instead of a centred one. Due to the refraction of rays of light on the free surface, the uppermost region of solitary waves centred at $x_0 = 0$ cannot be observed in the images. Recalling that half solitary waves exist in a particular region of parameter space, the frequency and amplitude of the external driving were suitably adjusted to $f = 10.97$ Hz and $\Gamma_0 = 0.127g$. Figures 3(*a*)
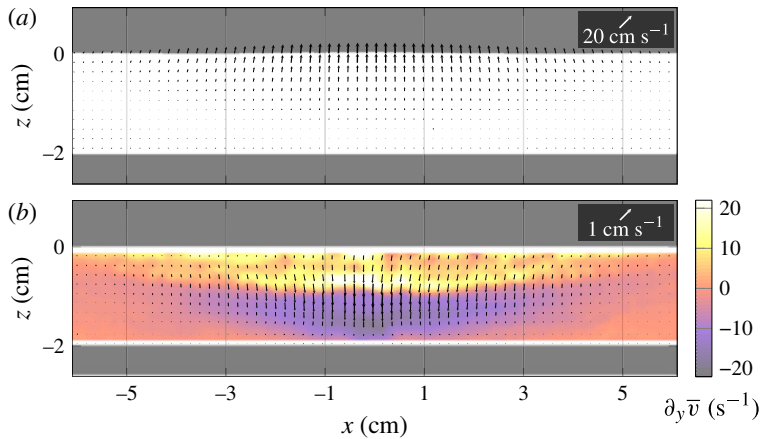
FIGURE 2. (Colour online) Front view (x–z plane) of the velocity field of a solitary wave whose envelope is centred at $x = 0$ and $\theta_s = \pi$. Only the central region of the trough is shown. The laser sheet is placed at $y_s = 1.07$ cm. (*a*) Instantaneous velocity field. (*b*) Streaming velocity field and out-of-plane velocity gradient $\partial_y \overline{v}$ (in colours). The scale of the arrows in each figure is also displayed.
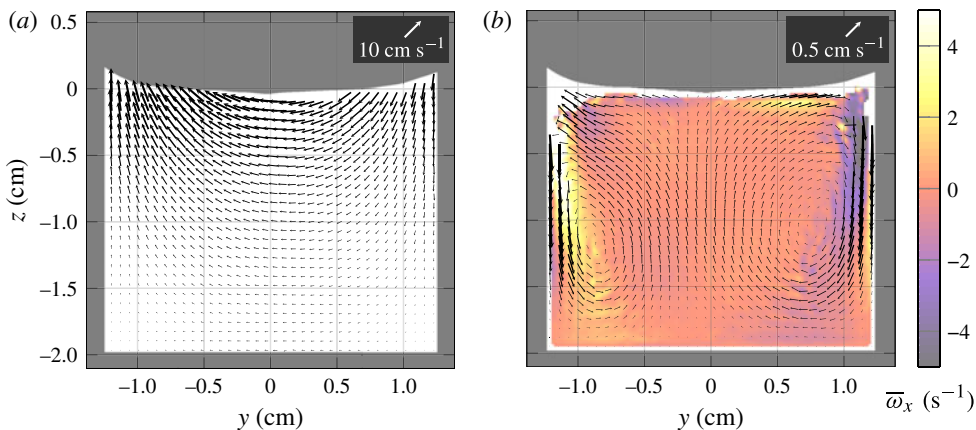

FIGURE 3. (Colour online) Side view (y–z plane) of the velocity field of a half solitary wave pinned at a lateral wall at $\theta_s = \pi$. The laser sheet was placed at $x_s = 9.23$ mm. (*a*) Instantaneous velocity field. (*b*) Streaming velocity field and out-of-plane vorticity $\overline{\omega}_x$ (in colours).

and (3*b*) display the corresponding instantaneous and streaming velocity fields. For both fields, the position of the laser sheet was $x_s = 9.23$ cm. With this side view, the zoomed images (1280 pixels $\times$ 1600 pixels in a 2.8 cm $\times$ 3.5 cm window; minimum interrogation window: 16 pixels $\times$ 16 pixels, i.e. 0.35 mm $\times$ 0.35 mm) allow us to resolve the menisci formed at the front and back walls. In the image, the white background represents regions occupied by the fluid. See the supplementary movies.

4.1. *Instantaneous velocity field*

The instantaneous velocity field inside the bulk of the parametrically excited solitary wave is comprised primarily of an oscillatory part. Before analysing any data, the

uniform velocity due to the driving of the basin was subtracted so that the velocity fields were in a frame of reference fixed to the basin. The front view of the velocity field shows that the motion is highly localized in the envelope of the structure with velocity magnitudes decreasing by one order of magnitude from the centre to the side walls of the trough. The magnitude of the velocity also increases on approach to the free surface, which is a general feature of gravity waves in uniform depth containers. These two spatial features can be observed throughout the entire cycle of the solitary wave: the direction of the arrows is largely time independent, i.e. only the magnitudes oscillate in time. Thus, a single-phase snapshot, as in figure 2(*a*), provides a representative example of the velocity distribution in the *x*–*y* plane. Furthermore, a quick inspection of the instantaneous velocity field in other planes by means of moving the laser sheet shows that the spatial and temporal features in the *x*–*z* plane are the same. Only the module of the arrows is reduced as one approaches the vertical centre of the basin.

This feature is in agreement with the velocity fields obtained from side views of the trough (*y*–*z* plane), as depicted in figure 3(*a*). The temporal features from this view match those from the *x*–*z* plane: a field with static orientation and time-oscillating magnitudes. The snapshots also display that particles move from the positive side of the *y* axis to the negative side as the free surface exhibits its characteristic sloshing motion. As expected, the magnitude of this motion increases when approaching the free surface.

4.2. *Streaming flow*

In contrast to the instantaneous velocity field, the streaming flow does not oscillate. By changing the phase of the light pulses with respect to the solitary-wave cycle, we observed that the field is essentially steady across the bulk of the fluid. An example of the velocity field in the *x*–*z* plane is shown in figure 2(*b*). The phase and y_s position of the illuminated plane are the same as for figure 2(*a*). It should be noticed that compared with the maximal instantaneous velocity, these magnitudes are around 20 times smaller. In this phase, we can observe that the particles are pushed downward and outward from the solitary-wave core. Higher magnitudes are observed in the centre of the channel rather than close to the free surface. The velocity field suggests an important out-of-plane velocity gradient (see the colours in figure 2*b*). Particles are streamed into the plane at the top and out of the plane at the bottom. The opposite occurs in the centre of the basin ($y_s = 0$), where particles move upward everywhere.

To clarify the general structure of the streaming motion of particles, the *y*–*z* view is very useful. The velocity field in figure 3(*b*) shows a pair of vortex-like structures aligned with the *x* axis. As observed in the *x*–*z* view, particles are streamed downward at the front and back walls ($y = \pm b/2$) and upward in the centre of the trough. Streaming near both menisci is hard to resolve since particle images are subject to a high shear in this region. The vorticity, defined as usual as $\boldsymbol{\omega} \equiv \nabla \times \boldsymbol{u}$, displays a noticeable out-of-plane component (shown in colours in figure 3*b*) and is highly localized near the front and back walls. The vorticity core is pinched to the meniscus and slightly pushed back by the walls as *z* decreases.

5. Discussion and conclusions

5.1. *Comparison with predicted results*

Generally speaking, the model of Miles (1984*b*), based on Hamiltonian equations and linear dissipation, satisfactorily predicts the deformation of the free surface of
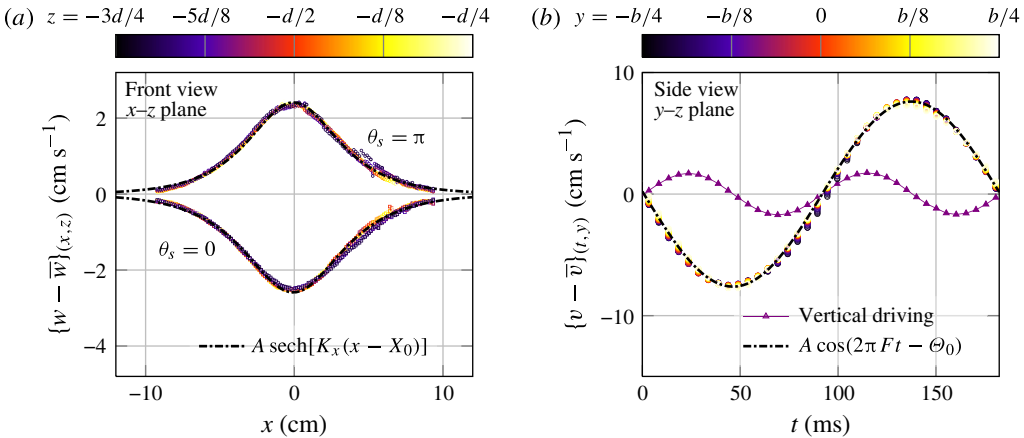
FIGURE 4. (Colour online) Surface fitting results of the potential model (5.1) for solitary waves. For visualization, surfaces are collapsed onto single master curves (symbols) which are then compared with fitted models (dash-dotted lines). (*a*) Maximal and minimal oscillatory vertical velocity $w - \overline{w}$ in the (x, z) plane. The fitting parameters for the upper curve are $A = 2.41 \pm 0.04$ cm s^{-1}, $K_x = 0.373 \pm 0.002$ cm^{-1}, $K_z = 1.36 \pm 0.01$ cm^{-1}, $X_0 = -0.06 \pm 0.01$ cm, and those for the lower curve are $A = -2.59 \pm 0.04$ cm s^{-1}, $K_x = 0.344 \pm 0.001$ cm^{-1}, $K_z = 1.24 \pm 0.01$ cm^{-1}, $X_0 = -0.08 \pm 0.01$ cm. (*b*) Oscillatory horizontal velocity $v - \overline{v}$ in the (y, t) plane. The fitting parameters are $A = 7.61 \pm 0.02$ cm s^{-1}, $f = 5.492 \pm 0.005$ Hz, $K_y = 1.21 \pm 0.01$ cm^{-1}, $\Phi_0 = -1.543 \pm 0.004$. The vertical velocity of the basin is also displayed.

parametrically excited solitary waves (see Clerc *et al.* 2009; Gordillo *et al.* 2011). We now compare this model with the velocity field inside the bulk of solitary waves. According to Miles' theory, the velocity of the fluid underneath the free surface is irrotational and satisfies $\widetilde{\boldsymbol{u}} = (\widetilde{u}, \widetilde{v}, \widetilde{w}) = \nabla \Phi$. The potential is given by

$$\Phi\,(x, y, z, t) = \frac{\pm a_s \delta g \sin ky \cosh k\,(z + d) \cos \theta_s(t)}{\omega_{01} \cosh kd \cosh \left[\delta b^{-1/2} k\,(x - x_0)\right]}, \tag{5.1}$$

where $\theta_s(t) = \omega t + \frac{1}{2} \sin^{-1}(\mu/\gamma)$. Equation (5.1) can be used to predict the components of the velocity field. Thus, a simple way to test the accuracy of the model is to fit it to the experimentally measured velocity field. To reduce the high dimensionality of the set of dependent variables (three for space and one for time), we fixed two dependent variables and applied a surface fit using the cftool function in Matlab on the remaining two.

In figure 4(*a*), we display the results for the oscillatory vertical velocity $\widetilde{w} = w - \overline{w}$ in the x–z plane. Here, y is fixed at $y_s = 1.07$ cm and t corresponds to the two phases at which the velocities are maximal and minimal, i.e. $\theta_s = \{0, \pi\}$. For visualization, we collapsed the PIV experimental data for eight different z values ($-1.5 < z < 0.5$ cm) into two master curves. This was done by dividing the data by the z-dependent part of $\partial_z \Phi$, i.e. $\sinh[K_z(z + d)]$. The curves should then be represented by a function $f(x) = A \operatorname{sech} K_x(x - X_0)$. Variables in capital letters are fitted parameters.

A similar comparison for the temporal evolution of the velocity field of a half parametrically excited solitary wave is displayed in figure 4(*b*). In this case, we analysed the oscillatory horizontal velocity from the side views, $\widetilde{v} = v - \overline{v}$, in

terms of the time t and the horizontal coordinate y at a fixed depth $z = -0.44$ cm (the x position is again fixed at $x_s = 9.23$ mm). For visualization, the surface in the (y, t) space was collapsed onto a single master curve by diving the velocity profiles by the y-dependence part $\partial_y \Phi$, i.e. $\cos[K_y y]$. A set of 80 curves in the range $-0.64 < y < 0.64$ cm were used for this purpose. According to (5.1), the velocity should be well fitted by $f(x) = A \cos(2\pi F t - \Theta_0)$. The vertical velocity of the basin is also plotted, displaying the parametric nature of the instability.

Figures 4(a) and (4b) provide compelling evidence that the potential-velocity model describes well the oscillatory part of the velocity field. The hyperbolic secant profiles reproduce with excellent accuracy the velocity distribution along the solitary wave. The fitted values for maximal and minimal vertical velocity $\widetilde{w} = (w - \overline{w})$ of figure 4(a) show good agreement. In general, the fitted values for K_y and K_z match the crosswise wavenumber $k = \pi/b = 1.24$ cm^{-1}. Accordingly, experimental measurements for the half solitary wave show a crosswise standing wave profile that oscillates harmonically at twice the driving period.

5.2. *Parametric streaming*

At this point, Miles' model seems to satisfactorily reproduce the experimental data, at least when comparisons with experimental data are made after subtracting the mean streaming velocity field from the instantaneous one. This important step of processing is vital for the agreement displayed in figure 4(a,b). Although Miles' model for Hamiltonian flows can yield some sort of streaming for higher-order terms (see Gordillo 2012), these corrections remain potential (i.e. $\omega = 0$) across the whole bulk of the fluid. Hence, the model is blind to streaming flows with vorticity distribution such as the one that parametrically excited solitary waves support. Even more striking is the fact that the streaming flow is so significant. Using (2.3) and the formulae for the pdNLSe parameters, we can estimate the following values from experimental data: $\psi \sim 10^{-1}$ and $\nu \sim \mu \sim \gamma \sim 10^{-1}$. Meanwhile, the ratio between the streaming and the potential velocities is $\overline{w}/w \approx 10^{-1}$. This means that the corrections due to the coupling of streaming and potential flow are ψ^3 and, consequently, as important as the higher-order term in (2.1), which is responsible for the highly localized envelope of the parametrically excited solitary wave. The question naturally arises of what the physical origin of the parametric streaming is.

5.2.1. *A simple model for parametric streaming*

The physical origin of streaming in parametric flows has been widely studied in a slightly different domain: acoustic flows. Streaming occurs because oscillatory boundary layers transfer vorticity to the bulk of the fluid. The induced streaming velocity field is independent of the viscosity of the fluid μ^* and does not vanish as $\mu^* \to 0$. This is a consequence of the singular limit of the Navier–Stokes equation at high Reynolds number. Streaming in parametric instabilities was first visualized by Douady (1990) using Kalliroscope particles in a Faraday-instability configuration. To the best of our knowledge, quantitative measurements of the streaming field in a parametric instability have never been reported. Theoretical analysis on this subject is also rare and has addressed the bottom and free-surface boundary layers (Longuet-Higgins 1953; Martín & Vega 2005). Since parametrically excited solitary waves must be supported between two vertical walls, we are sceptical about their applicability to our set-up.

To understand how vorticity is induced in the bulk through the streaming flow, we analyse the Navier–Stokes equation for vorticity (ν^* is the kinematic viscosity of the fluid),

$$\partial_t \boldsymbol{\omega} + \boldsymbol{\nabla} \times (\boldsymbol{u} \times \boldsymbol{\omega}) = \nu^* \nabla^2 \boldsymbol{\omega}, \tag{5.2}$$

which is complemented with the incompressible flow equation $\boldsymbol{\nabla} \cdot \boldsymbol{u} = 0$. Following our experimental results for the bulk, we assume that the field $\boldsymbol{u}$ and the vorticity $\boldsymbol{\omega}$ are comprised of two terms: a leading-order oscillatory part and a second-order streaming (steady) part. Since the oscillatory part of the bulk vorticity $\widetilde{\boldsymbol{\omega}}$ is derived from a potential velocity field $\widetilde{\boldsymbol{u}}$, it follows that $\widetilde{\boldsymbol{\omega}} = 0$. Indeed, if (5.2) is integrated during a cycle, the nonlinear terms coupling the oscillatory and the streaming flow also vanish. The equation for the streaming vorticity across the bulk then reads

$$\partial_t \overline{\boldsymbol{\omega}} + (\overline{\boldsymbol{u}} \cdot \boldsymbol{\nabla}) \, \overline{\boldsymbol{\omega}} - (\overline{\boldsymbol{\omega}} \cdot \boldsymbol{\nabla}) \, \overline{\boldsymbol{u}} = \nu^* \nabla^2 \overline{\boldsymbol{\omega}}. \tag{5.3}$$

The first term represents a slow temporal evolution of the streaming vorticity and is dominant over the neglected nonlinear terms. In contrast to the calculations in Martín, Martel & Vega (2002) for slowly propagating waves in unbounded basins, our oscillatory flow does not couple with the streaming one in the bulk through a Stokes drift term. Coupling is exclusively achieved via the boundary layers along the rigid walls and the free surface, which require a completely separate analysis using boundary layer techniques. A suitable analysis for a rigid wall subject to an external tangential velocity field oscillating at ω can be found in Batchelor (2000, pp. 358–361). The theory predicts shear layers of extent $\delta_\nu \sim \sqrt{2\nu/\omega}$. In our experiments, this quantity ($\delta_\nu \approx 20$ µm) is two orders of magnitude smaller than the spatial features of the potential flow ($b = 2$ cm), which is consistent with oscillatory boundary layer hypotheses. The theory also predicts that if the outer oscillatory velocity can be written as $\mathrm{Re}\{\widetilde{\boldsymbol{u}}^{out} \exp[\mathrm{i}\omega t + \mathrm{i}\varphi]\}$ (the amplitude $\widetilde{\boldsymbol{u}}^{out}$ and phase φ may have spatial dependence), the spatial asymptotic matching condition on the outer streaming velocity is (cf. Gordillo 2012)

$$\overline{\boldsymbol{u}}^{out} = -\frac{1}{4\omega} \left\{ \left(\widetilde{\boldsymbol{u}}^{out} \cdot \boldsymbol{\nabla} \right) \widetilde{\boldsymbol{u}}^{out} + 2 \left(\boldsymbol{\nabla} \cdot \widetilde{\boldsymbol{u}}^{out} \right) \widetilde{\boldsymbol{u}}^{out} + 3 \left[\left(\widetilde{\boldsymbol{u}}^{out} \cdot \boldsymbol{\nabla} \right) \gamma \right] \widetilde{\boldsymbol{u}}^{out} \right\}. \tag{5.4}$$

In practical terms, the coupling at the boundary layers arises from the convective nonlinear terms, which are quadratic and allow steady resonances of the form $\sim \exp(\mathrm{i}\omega t) \times \exp(-\mathrm{i}\omega t)$. It should be noticed also that both outer velocities, $\overline{\boldsymbol{u}}^{out}$ and $\widetilde{\boldsymbol{u}}^{out}$, are tangential to the wall in agreement with impermeability boundary conditions. Remarkably, the induced streaming velocity does not depend at all on the kinematic viscosity, which is a direct consequence of the singular limit of the Navier–Stokes equations as the Reynolds number $Re \longrightarrow \infty$.

For a free surface subject to an external oscillatory velocity field, the boundary layer analysis provides a different type of result: instead of imposing an outer tangential streaming field as in (5.4), the constraint applies to the tangential-stress condition, which should be zero. In terms of the velocity field, the spatial asymptotic matching condition can be written as

$$\frac{\partial}{\partial n} \overline{\boldsymbol{u}}_{\parallel}^{out} = 0, \quad \overline{\boldsymbol{u}}_{\perp}^{out} = 0, \tag{5.5a,b}$$

where the second equation comes from the impermeability condition at the free surface. Remarkably, (5.3)–(5.5), together with the mass conservation equation for

the streaming part, $\nabla \cdot \overline{\boldsymbol{u}} = 0$, constitute an independent set of dynamic equations for the streaming velocitiy and vorticity in the bulk. The coupling with the dominant oscillating flow only appears in asymptotic matching conditions on the boundaries, i.e. (5.4), which can now be regarded as classical boundary conditions.

The previous analysis can be applied for any type of three-dimensional oscillatory potential flow. For parametrically excited solitary waves, the problem can be simplified further: the slight dependence of the solution along the x direction (see e.g. the velocity in figure 2) suggests that the streaming field is dominated by y–z components, i.e. $\overline{\boldsymbol{u}} \approx (0, \overline{v}, \overline{w})$, and that the vorticity's main component lies along the x direction, i.e. $\overline{\boldsymbol{\omega}} \approx \omega \boldsymbol{i}$. The configuration can thus be considered as two-dimensional (the x dependence can be considered as a simple slow modulation of the two-dimensional problem). Considering a stream function Ψ such that $(0, \overline{v}, \overline{w}) = \nabla \times (\Psi \boldsymbol{i})$, the problem can be written as

$$\partial_t \omega + \partial_z \Psi \partial_y \omega - \partial_y \Psi \partial_z \omega = \nu \nabla^2 \omega, \tag{5.6}$$

$$\omega = -\nabla^2 \Psi. \tag{5.7}$$

The spatial asymptotic matching conditions for the parametrically excited solitary wave can be easily obtained from (2.3), (5.4) and (5.5). For the rigid boundaries, we obtain Dirichlet boundary conditions for the tangential velocities

$$\overline{v}|_{z=-d} = \left. -\frac{3}{4\omega} \partial_y \Phi \, \partial_{yy} \Phi \right|_{z=-d} = -\frac{3 a_s^2 \, |\psi|^2 \, \omega k}{8} \frac{\sin 2ky}{\sinh^2 kd}, \tag{5.8}$$

$$\overline{w}|_{y=\pm b/2} = \left. -\frac{3}{4\omega} \partial_z \Phi \, \partial_{zz} \Phi \right|_{y=\pm b/2} = -\frac{3 a_s^2 \, |\psi|^2 \, \omega k}{8} \frac{\sinh 2k \, (z+d)}{\sinh^2 kd}, \tag{5.9}$$

for the bottom and the front and back walls respectively. On the other hand, the zero-tangential-stress condition on the free surface is satisfied with the Neumann boundary condition for the tangential velocity

$$\partial_z \overline{v}|_{z=0} = 0. \tag{5.10}$$

The impermeability conditions on the wall and the free surface fix Dirichlet boundary conditions for all the normal components of velocity along the boundaries,

$$\overline{w}|_{z=-d} = \overline{v}|_{y=\pm b/2} = \overline{w}|_{z=0} = 0. \tag{5.11}$$

Equations (5.6)–(5.11) are the same as those of a two-dimensional driven-cavity problem with a static free surface at $z = 0$. The front, back and bottom boundaries can be thought of as a series of moving belts with time-steady but spatially non-uniform velocities.

To solve the system of partial differential equations (PDEs) in the domain $\Omega = \{(y, z) \mid |y| < b/2, -1 < z < 0\}$, we implemented a numerical routine similar to that proposed in Tannehill, Anderson & Pletcher (1997, pp. 650–652). The routine is a time-marching algorithm that uses a classical finite-difference scheme for elliptic PDEs. At each time step n:

(a) the stream function $\Psi^{(n)}$ in the bulk is solved using Poisson's equation (5.7) and the vorticity at the previous step, $\omega^{(n-1)}$, via a succesive over-relaxation method (SOR);

(b) the stream function along the boundaries, $\Psi^{(n)}|_{\partial\Omega}$, is fixed to zero, enforcing mass conservation (boundaries are streamlines throughout);

(c) the vorticity along the boundaries, $\omega^{(n)}|_{\partial\Omega}$, is obtained at second-order precision using the boundary conditions (5.8)–(5.11) and the previously calculated values for $\Psi^{(n)}$;

(d) the vorticity $\omega^{(n)}$ in the bulk is calculated using the vorticity-transport equation (5.6) and the vorticity at the previous step, $\omega^{(n-1)}$, by means of a forward Euler scheme.

The numerical simulations were run on a 128×201 uniform mesh, which fits the half of the domain Ω (ω and Ψ are antisymmetric along the axis $y = 0$, so $\omega|_{y=0} = \Psi|_{y=0} = 0$). The kinematic viscosity used for simulations, $\nu^* = 0.85$ cSt, was chosen to match the value of the KBr aqueous solution described in §3. The values for k, d and ω are obtained from formulae in §2, while the factor $a_s|\psi|$ in (5.8) and (5.9) was estimated from the contact-line maximal height in images, i.e. $a_s|\psi| = 0.59$ cm. The initial condition was chosen to be $\Psi^{(0)} = \omega^{(0)} = 0$. Finally, we fixed the time step at $\Delta t = 4.5$ µs, after checking that the solutions converge as $\Delta t \longrightarrow 0$.

In figure 5(a–d), we display our results from numerical simulations: the out-of-plane vorticity ω and a set of streamlines are shown as time t evolves (results for the $y < 0$ plane are used for building a solution in the whole domain Ω using the Ψ–ω symmetry properties). As shown in figure 5(a), after just a few time steps, the vorticity is rapidly introduced into the fluid bulk from two sources: (i) the contact-line points, i.e. $(y, z) = (\pm b/2, 0)$, and (ii) the half-bottom centres, $(y, z) = (\pm b/4, -d)$. The main stream is due to the former, which impose two large counter-rotating eddies that carry fluid particles downward along the walls, and then upward along the cavity centre. The other stream, due to the bottom boundary layer, also consists of two counter-rotating eddies, but carries fluid in the other direction. This stream is very weak compared with the main one, and its size is smaller. The direction of this weak stream (upward velocity in the stationary-wave node at $y = 0$) is consistent with the experimental observations in Douady (1990) for Faraday waves in large basins and the theoretical results in Longuet-Higgins (1953) for periodic basins. As time evolves from figures 5(a) to (5c), vorticity is continuously diffused toward the bulk until the solution converges to a steady state in figure 5(d). During this process, the centres of the main counter-rotating eddies (at which Ψ is maximal or minimal) drift slowly to the centre of the basin while their outer streamlines increase in size. Meanwhile, the weak bottom eddies shrink continuously into thin layers.

When compared with experimental results, i.e. the vorticity in figure 3(b) and the particle tracks (streamlines) in figure 5(d), the parametric streaming model seems to fit the observed results well. The direction of the streaming is correctly predicted, as well as the apparent overturning of the bottom boundary layers observed by Douady (1990). The vorticity distribution, including the high-shear regions near the contact line, is also quantitatively close to the experimental outcome. However, there are still some differences, e.g. the experimental streamlines are more pinched to the contact line in the early stages of the vorticity evolution (see figure 5b). The asymmetry in the streaming pattern may be due to slight differences in the roughness of the vertical walls (this should be controlled better in further experiments). We think that these finer differences could be due to (i) the lack of a meniscus in the simulated domain Ω, (ii) the three-dimensional character of the parametrically excited solitary wave and (iii) the neglect of the oscillating contact line. While the features (i) and (ii) could be solved using more complex numerical codes, (iii) requires one to address a more
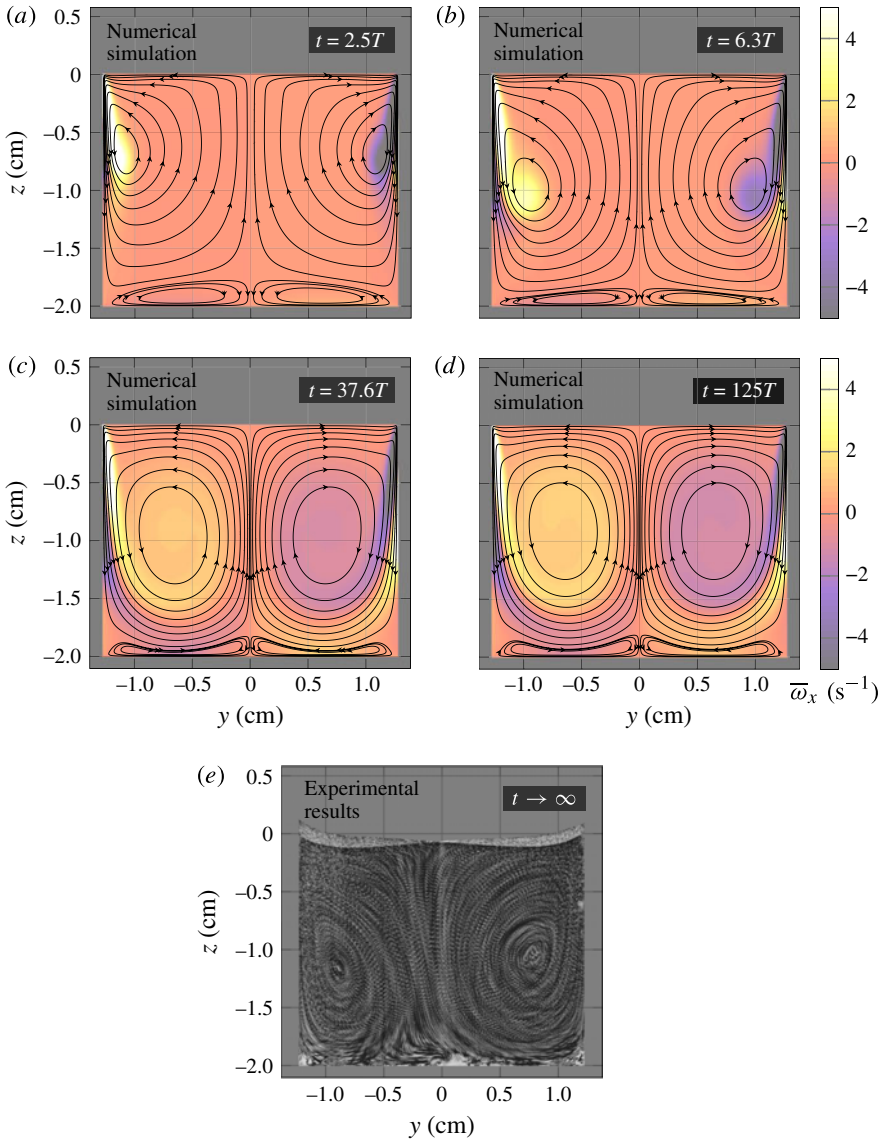
FIGURE 5. (Colour online) From (*a*) to (*d*): out-of-plane vorticity and streamlines for the parametric streaming model at several times *t*. The dimensions of the cell, the fluid parameters and the cross-wave parameters match those of the side-view experiments without any fitting parameter. In (*d*), the stationary state of the vorticity-transport equations is shown. In (*e*), we display the particle tracks obtained by averaging a series of stroboscopic images in the steady streaming state. Particle tracks can be considered as experimental streamlines.

fundamental hydrodynamical problem: to understand and be able to predict boundary layer streaming near oscillatory contact lines. In any case, it is very surprising to see that the simple model that we propose is able to capture the main features of the streaming flow in spite of the advancing and receding menisci phemenon.

5.2.2. *Parametric streaming in the pdNLSe*

A natural question that follows is why Miles' model and the pdNLSe have been so successful in describing parametrically excited solitary waves despite the fact that they do not consider the streaming we observe in our experiments. Theoretical works on this subject can give us some important clues. Martín *et al.* (2002) considered the problem of finding an amplitude equation for two-dimensional Faraday waves starting from the Navier–Stokes equation in a laterally unbounded fluid. The resulting amplitude equation is similar to that obtained from Hamiltonian formulations (Miles 1984*a*) except for an integral term that accounts for the coupling between streaming and the Faraday waves. This term does not generate a major change in the general dynamics of the amplitude equation although it is vital to explain drift instability in Faraday waves (Martín *et al.* 2002). For parametrically excited solitary waves, although the calculations are considerably more complex, streaming coupling should provide corrections to the a_s factor, defined after (2.2) and (2.3), without modifying the dynamics of the pdNLSe. However, it is hard to establish the scope of this coupling term for further bifurcations. In order to meet the challenge of explicitly incorporating parametric streaming in the amplitude equation for parametrically excited solitary waves, we should attempt first to find a closed-form solution of the § 5.2.1 nonlinear model in terms of the local value of ψ.

Acknowledgements

Supplementary movies

Supplementary movies are available at http://dx.doi.org/10.1017/jfm.2014.416.

REFERENCES

ARBELL, H. & FINEBERG, J. 2000 Temporally harmonic oscillons in Newtonian fluids. *Phys. Rev. Lett.* **85** (4), 756–759.

BARASHENKOV, I. V., BOGDAN, M. M. & KOROBOV, V. I. 1991 Stability diagram of the phase-locked solitons in the parametrically driven, damped nonlinear Schrödinger equation. *Europhys. Lett.* **15**, 113–118.

BATCHELOR, G. K. 2000 *An Introduction to Fluid Dynamics*. Cambridge University Press.

CHEN, W., TU, J. & WEI, R. 1999 Onset instability to non-propagating hydrodynamic solitons. *Phys. Lett.* A **255** (4), 272–276.

CLERC, M. G., COULIBALY, S., GORDILLO, L., MUJICA, N. & NAVARRO, R. 2011 Coalescence cascade of dissipative solitons in parametrically driven systems. *Phys. Rev. E* **84** (3), 036205.

CLERC, M. G., COULIBALY, S., MUJICA, N., NAVARRO, R. & SAUMA, T. 2009 Soliton pair interaction law in parametrically driven Newtonian fluid. *Phil. Trans. R. Soc. Lond.* A **367**, 3213–3226.

DENARDO, B., GALVIN, B., GREENFIELD, A., LARRAZA, A., PUTTERMAN, S. J. & WRIGHT, W. B. 1992 Observations of localized structures in nonlinear lattices: domain walls and kinks. *Phys. Rev. Lett.* **68** (1), 1730–1733.

DENARDO, B., WRIGHT, W. B., PUTTERMAN, S. J. & LARRAZA, A. 1990 Observation of a kink soliton on the surface of a liquid. *Phys. Rev. Lett.* **64** (1), 1518–1521.

DOUADY, S. 1990 Experimental study of the Faraday instability. *J. Fluid Mech.* **221**, 383–409.

GORDILLO, L. 2012 Non-propagating hydrodynamic solitons in a quasi-one-dimensional free surface subject to vertical vibrations. PhD thesis, Universidad de Chile, Santiago.

GORDILLO, L., SAUMA, T., ZÁRATE, Y., ESPINOZA, I., CLERC, M. G. & MUJICA, N. 2011 Can non-propagating hydrodynamic solitons be forced to move? *Eur. Phys. J.* D **62** (1), 39–49.

LAEDKE, E. W. & SPATSCHEK, K. H. 1991 On localized solutions in nonlinear Faraday resonance. *J. Fluid Mech.* **223**, 589–601.

LIDE, D. R. 2004 *Handbook of Chemistry and Physics*, 85th edn. Chemical Rubber Company Press.

LONGUET-HIGGINS, M. S. 1953 Mass Transport in Water Waves. *Phil. Trans. R. Soc. Lond.* A **245**, 535–581.

MARTÍN, E., MARTEL, C. & VEGA, J. M. 2002 Drift instability of standing Faraday waves. *J. Fluid Mech.* **467**, 57–79.

MARTÍN, E. & VEGA, J. M. 2005 The effect of surface contamination on the drift instability of standing Faraday waves. *J. Fluid Mech.* **546**, 203–225.

MILES, J. W. 1967 Surface-wave damping in closed basins. *Proc. R. Soc. Lond.* A **297**, 459–475.

MILES, J. W. 1976 Nonlinear surface waves in closed basins. *J. Fluid Mech.* **75**, 419–448.

MILES, J. W. 1977 On Hamilton's principle for surface waves. *J. Fluid Mech.* **83**, 153–158.

MILES, J. W. 1984a Nonlinear Faraday resonance. *J. Fluid Mech.* **146**, 285–302.

MILES, J. W. 1984b Parametrically excited solitary waves. *J. Fluid Mech.* **148**, 451–460.

RAJCHENBACH, J., LEROUX, A. & CLAMOND, D. 2011 New standing solitary waves in water. *Phys. Rev. Lett.* **107** (2), 024502.

SANCHIS, A. & JENSEN, A. 2011 Dynamic masking of PIV images using the Radon transform in free surface flows. *Exp. Fluids* **51** (4), 871–880.

TANNEHILL, J., ANDERSON, D. & PLETCHER, R. 1997 *Computational Fluid Mechanics and Heat Transfer*, 2nd edn. Taylor & Francis.

UMEKI, M. 1991 Parametric dissipative nonlinear Schrödinger equation. *J. Phys. Soc. Japan* **60** (1), 146–167.

WANG, W., WANG, X., WANG, J. & WEI, R. 1996 Dynamical behavior of parametrically excited solitary waves in Faraday's water trough experiment. *Phys. Lett.* A **219**, 74–78.

WANG, X. & WEI, R. 1994 Observations of collision behavior of parametrically excited standing solitons. *Phys. Lett.* A **192** (1), 1–4.

WU, J., KEOLIAN, R. & RUDNICK, I. 1984 Observation of a non-propagating hydrodynamic soliton. *Phys. Rev. Lett.* **52** (1), 1421–1424.

ZHANG, L., WANG, X. & TAO, Z. 2007 Spatiotemporal bifurcations of a parametrically excited solitary wave. *Phys. Rev.* E **75** (3), 036602.